Controlling the Hydrophilicity of the Electrochemical Interface to Modulate the Oxygen-Atom Transfer in Electrocatalytic Epoxidation Reactions

Florian Dorchies[1,2], Alessandra Serva[2,3], Dorian Crevel[2,4], Jérémy De Freitas[5], Nikolaos Kostopoulos[5], Marc Robert[5,6], Ozlem Sel[1,2], Mathieu Salanne[2,3,6], and Alexis Grimaud[1,2,7]*

[1] Chimie du Solide et de l'Energie, UMR 8260, Collège de France, 75231 Paris Cedex 05, France

[2] Réseau sur le stockage Electrochimique de l'Energie (RS2E), CNRS FR3459, 80039 Amiens Cedex, France

[3] Sorbonne Université, CNRS, Physicochimie des Électrolytes et Nanosystèmes Interfaciaux, PHENIX, F-75005 Paris, France

[4] Université Paris-Saclay, Univ Evry, CNRS, LAMBE, 91025, Evry-Courcouronnes, France

[5] Laboratoire d'Electrochimie Moléculaire, Université de Paris, CNRS, F-75006 Paris, France

[6] Institut Universitaire de France (IUF), 75231 Paris, France

[7] Department of Chemistry, Merkert Chemistry Center, Boston College, Chestnut Hill, MA

*Correspondence to alexis.grimaud@bc.edu

ABSTRACT

The electrocatalytic epoxidation of alkenes at heterogeneous catalysts using water as the sole oxygen source is a promising safe route toward the sustainable synthesis of epoxides, which are essential building blocks in organic chemistry. However, the physico-chemical parameters governing the oxygen-atom transfer to the alkene and the impact of the electrolyte structure on the epoxidation reaction are yet to be understood. Here, we study the electrocatalytic epoxidation of cyclooctene at the surface of gold in hybrid organic/aqueous mixtures using acetonitrile (ACN) solvent. Gold was selected, as in ACN/water electrolytes gold oxide is formed by reactivity with water at potentials less anodic than the oxygen evolution reaction (OER). This unique property allows us to demonstrate that a sacrificial mechanism is responsible for cyclooctene epoxidation at metallic gold surfaces, proceeding through cyclooctene activation, while epoxidation at gold oxide shares similar reaction intermediates with the OER and proceeds via the activation of water. More importantly, we show that the hydrophilicity of the electrode/electrolyte interface can be tuned by changing the nature of the supporting salt cation, hence affecting the reaction selectivity. At low overpotential, hydrophilic interfaces formed by using strong Lewis acid cations are found to favor gold passivation. Instead, hydrophobic interfaces created by the use of large organic cations favor the oxidation of cyclooctene and the formation of epoxide. Our study directly demonstrates how tuning the hydrophilicity of electrochemical interfaces can improve both the yield and selectivity of anodic reactions at the surface of heterogeneous catalysts.

INTRODUCTION

The past decades have seen a growing interest in the development of electrosynthesis as a powerful synthetic tool. This is because, beyond its innate sustainability when powered by renewables,[1,2] electrosynthesis possesses many advantages such as high functional group tolerance, mild conditions, ability to selectively conduct oxidation and reduction reactions at controlled potentials and scalability.[2–5] Numerous anodic and cathodic reactions have been developed, allowing the forging of useful chemical bonds,[2–11] the chemoselective functionalization of peptides and proteins[12] and even the total synthesis of natural products for which chemical synthesis has no practical solution.[13] Among these reactions, electrochemical oxygenation reactions are of particular interest as they allow for the direct and chemoselective functionalization of C-H and C=C bonds forming industrially and pharmaceutically relevant chemical functions such as enones,[14] ketones,[15–22] aldehydes,[16,19,23] lactams,[24] lactones,[25] alcohols[15,21,22,26] and epoxides.[21,22,27–38] The efficient and environmentally friendly preparation of an epoxide moiety is of prime importance as this structure is found in numerous natural products with potential biological activities,[39–41] is a versatile building block in organic chemistry[41,42] and plays an important role in industry.[11,43]

Electrochemical epoxidation methods currently proceed via the anodic activation of molecular complexes,[20,35,44] thus complicating the isolation of the final product, or via the *in situ* generation of hazardous oxidants such as Cl_2, Br_2 and H_2O_2.[21,28,32,34,36,38] Recently, an electrocatalytic epoxidation strategy using water as the sole oxygen source and a manganese oxide electrocatalyst to heterogeneously transfer the oxygen to the alkene was proposed to circumvent the aforementioned drawbacks.[27,30] However, little is known regarding the role of the electrocatalyst on the oxygen-atom transfer and more precisely on the parameters governing the selectivity

between the oxygen evolution reaction (OER) and the epoxidation, which are pivotal for increasing the efficiency of the later process. In particular, questions arise regarding the exact role of the oxygen ligand at the surface of the electrocatalyst on the oxygen-atom transfer to the alkene. Indeed, conflicting results exist in the literature, with studies postulating that oxygen ligand is involved in the oxygen transfer[27,29,30,45] and others not.[17,26] For the competing reaction involving water oxidation, i.e. the OER, it was recently shown that the involvement of the oxygen ligand into the O-O bond formation boosts the kinetics of the anodic reaction,[46,47] metal-oxygen bond covalency and O 2*p* band levels serving as descriptors for the reaction.[46,48] Knowing that, one may wonder if similar physical properties can describe the oxygen-atom transfer in epoxidation reactions, and maybe more importantly if activating oxygen ligands from the catalyst could decrease the selectivity of the epoxidation reaction by favoring the OER.

Aside from questions regarding the implication of oxygen ligands, the use of homogeneous mixtures of organic solvent and water is required, with the organic solvent serving to solubilize alkenes while water acts as co-reactant. In acetonitrile (ACN)/water mixtures, the most commonly employed mixtures,[17,25,27,30,49] aqueous and organic domains exist at the nanoscale.[50] These domains are conserved at the catalyst/electrolyte interface and were shown to modulate water reduction.[50] As recently proposed in a theoretical study,[51] such nanodomains may play a significant role in tuning the selectivity and efficiency of electrochemical reactions. In this connection, one may note that the nature of the supporting salt cation is known to alter both the selectivity and kinetics of complex anodic reactions, such as electrohydrodimerization reactions,[52] but also the OER itself. Hence, recent studies have shown that large and hydrophobic cations block the OER[53] while strong Lewis acids such as Li^+ are detrimental to the OER because of the strong cation-OH_2 interaction.[53,54] Finding the optimal electrolyte composition favoring the oxygen-atom transfer to

alkenes while slowing down the OER may thus represent a unique opportunity to make electrochemical oxygenation reactions closer to industrial relevance.

Overall, we aim at applying methodologies and knowledge gathered in the past few years regarding the effect of catalysts' physical properties and ion adsorption at the solid/liquid interface to gain further insights into complex electrosynthetic processes. Herein we study an archetypal anodic oxygenation reaction, the electrocatalytic epoxidation of cyclooctene in ACN/water mixtures (Scheme 1).[27,30] To examine the role played by the surface of the electrocatalyst on the oxygen-atom transfer, we aimed for a single surface that can possess, or not, oxygen ligands as a function of cycling conditions. For that, gold was selected as in ACN/water mixtures, gold oxide is formed at potentials less positive than the OER,[55,56] allowing for investigating the epoxidation process both at a metallic surface and at a metal oxide surface. By combining rotating disk electrode measurements, electrochemical quartz crystal microbalance (EQCM), gas chromatography – mass spectrometry (GC-MS), inductively coupled plasma mass spectrometry (ICP-MS) and classical molecular dynamics (MD) simulations both in bulk and at electrified interfaces, we demonstrate that two different epoxidation mechanisms exist depending on the potential range. We show that a sacrificial mechanism is responsible for cyclooctene epoxidation at gold metallic surfaces while epoxidation at gold oxide shares similar reaction intermediates with the OER. Furthermore, we show that the mechanism at low overpotentials, i.e. the one at metallic gold, is strongly impacted by the electrolyte composition when changing the supporting salt cation, arising from a modification of the hydrophilicity of the electrode/electrolyte interface as a function of the nature of the cation. Alike what was recently demonstrated for the hydrogen evolution reaction,[50,57,58] our study thus reveals that the nature of the supporting salt cation in nanostructured electrolytes can modulate the kinetics and selectivity of catalytic reactions such as the epoxidation.

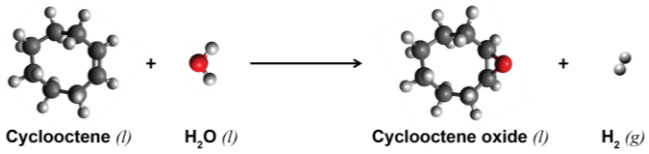

Scheme 1. Electrochemical cyclooctene epoxidation with water as the sole oxygen source.

RESULTS AND DISCUSSION

Electrochemistry of gold in acetonitrile/water/cyclooctene mixtures. The ACN to water ratio and the cyclooctene concentration were selected as those reported to give the highest epoxidation yield: ACN containing 5 M water, 0.1 M supporting salt and 200 mM cyclooctene.[27] Tetrabutylammonium perchlorate ($TBAClO_4$) was initially selected as supporting salt. The electrochemical behavior of polycrystalline gold in ACN/5 M water mixtures was first investigated in the presence or the absence of cyclooctene. Cyclic voltammograms recorded at 10 $mV.s^{-1}$ under rotation show two distinct features: a redox peak located at ~ 1.5 V vs the standard hydrogen electrode (SHE) followed by an anodic current with an onset potential of ~ 1.9 V vs SHE associated to the OER (Figure 1a), as previously reported in ACN/water mixtures.[55,56] It is noteworthy that the OER current is not affected by the presence of cyclooctene, the implications of which will be discussed below. On the contrary, the redox peak at ~ 1.5 V vs SHE is strongly affected by cyclooctene, with an onset potential shifted by 70 mV cathodically and an anodic Faradaic charge passed (Q_{ox}) in the presence of cyclooctene ~ 40 times greater than in the absence of cyclooctene (at 10 $mV.s^{-1}$). As previously discussed,[55] two ill-defined redox processes are simultaneously occurring at ~ 1.5 V vs SHE in ACN/water mixtures: gold dissolution into the electrolyte (reaction (1)) and gold oxide formation at the surface of the electrode (reaction (2)).

$$Au \rightarrow Au^{n+} + n\,e^{-} \quad (1)$$

$$Au + x\ H_2O\ \rightarrow AuO_x + 2x\ H^+ + 2x\ e^- \quad (2)$$

When cycling between 1.2 and 2.2 V vs SHE, the redox peak disappears after the first cycle, confirming the passivation of the electrode due to the formation of gold oxide following (2) (Figure S1). Gold dissolution in ACN/5 M water was monitored by inductively coupled plasma mass spectrometry (ICP-MS) measurements of the electrolyte after cycling at different scan rates. The amount of gold in solution is found to increase when the scan rate decreases, alike the charge passed Q_{ox} (Figure S2a). Gold dissolution is substantial in ACN/5 M water, with the equivalent of 5 monolayers dissolved when cycling at 100 $mV.s^{-1}$ and up to more than 150 at 1 $mV.s^{-1}$ (Figure S2b). In the presence of cyclooctene, Q_{ox} is much greater than in the absence of cyclooctene, with the ratio between both drastically increasing when the scan rate decreases (Figure 1b), suggesting that cyclooctene is involved in gold dissolution. The potential effect of dissolved chloride anions in the electrolyte, either coming from leakage from the reference electrode or impurities from the perchlorate salts, known to alter gold electrochemistry, was discarded (see Methods and Figure S3).[59,60]

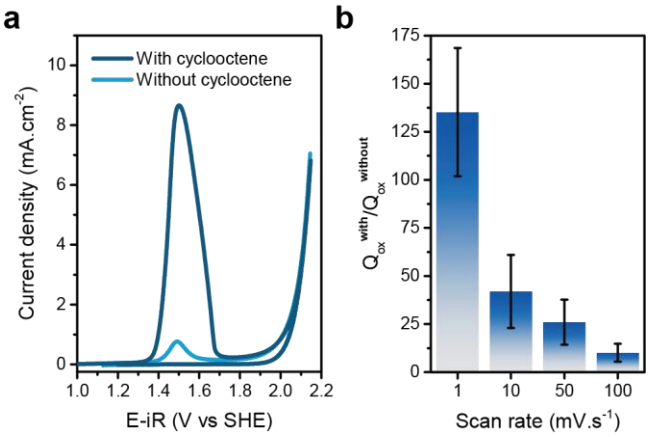

Figure 1. (a) Cyclic voltammograms obtained at a rotating gold electrode in ACN/water mixture in the presence (dark blue) or in the absence (light blue) of cyclooctene. WE: polycrystalline gold, CE: Pt wire, Ref: leakless Ag/AgCl, Ar-saturated ACN/5 M water/0.1 M $TBAClO_4$/0 or 200 mM cyclooctene, 10 $mV.s^{-1}$, 1,600 rpm. (b) Ratio of the charge associated to the redox peak at 1.5 V vs SHE (Q_{ox}) with and without cyclooctene as a function of scan rate. Error bars were obtained by repeating the experiments three times for each scan rate.

To further understand the effect of cyclooctene on gold dissolution and on the formation of gold oxide, electrochemical quartz crystal microbalance (EQCM) experiments were carried out. EQCM experiments were performed at 1 $mV.s^{-1}$, scan rate at which the Q_{ox} ratio with and without cyclooctene is the greatest (Figure 1b). Figure 2a shows that upon cycling in the 1.0 – 1.8 V vs SHE window in the absence of cyclooctene (red curves), the anodic peak is concomitant with an increase in frequency of the quartz resonator (~ 550 Hz), indicating a net loss of mass.[61] The frequency then stabilizes and remains stable during the reverse scan. Although gold oxide is formed at the surface of the gold electrode, frequency response shows a net increase (i.e. no gain of mass), indicating that gold dissolution is the predominant process in ACN/5 M water mixtures. This is in sharp contrast with the EQCM response of gold in aqueous electrolytes, where gold dissolution is very low and the gold oxide formation consequently leads to a decrease in the frequency of the quartz resonator (shown for 0.1 M $HClO_4$ in Figure S4). In the presence of cyclooctene (blue curves), the variation of frequency is ~ 18 times larger than without cyclooctene, in good agreement with Q_{ox} which is ~ 16 times more important than without cyclooctene. This

result indicates that cyclooctene mainly affects gold dissolution. Considering a plausible roughening of the surface of the gold electrode of the quartz resonators due to the substantial gold dissolution, the Sauerbrey equation was not applied to convert frequency variations into mass variations.[62,63] Complementary to the EQCM results, ICP-MS measurements show that the quantity of gold dissolved into the electrolyte is much higher in the presence of cyclooctene (Figure 2b). Along with the cathodic shift observed for the onset potential for gold dissolution (Figure 1a), EQCM and ICP-MS results show that cyclooctene drives the dissolution of gold into the electrolyte, likely due to its mild chelating effect.[64] This assumption is further supported by comparing the results obtained using 1,5-cyclooctadiene, a better chelating ligand for gold cations,[64,65] with that recorded for cyclooctene. In the presence of 1,5-cyclooctadiene, electrochemical and ICP-MS experiments show that the gold dissolution into the ACN/5 M water mixture is even more dramatic (Figure S5).

The substantial dissolution of gold is accompanied by a change of color of the electrolyte, which becomes dark purple (Figure S6). The UV-vis spectrum of the electrolyte taken after performing an anodic CV scan in the presence of cyclooctene is characteristic of spherical gold nanoparticles (NPs) with a surface plasmon resonance peak at λ=565 nm (Figure 2c, light purple). From the value of the surface plasmon resonance, the size of the NPs can be estimated to be ~ 100 nm,[66] in agreement with the dark purple color of the electrolyte. Interestingly, the absorbance of the solution increased after 30 minutes, while the value of the surface plasmon resonance remained constant (Figure 2c, dark purple). This observation indicates an increase of the number of gold NPs but not of their size.[67] Moreover, rotating ring disk electrode measurements show that the gold species generated at the disk can be reduced at the Pt ring (Figure S7 and S8), revealing the presence of gold cations formed upon dissolution. The most likely phenomenon at play is thus that unstable

gold cations are generated upon gold dissolution, the exact nature being outside of the scope of this study (no clear result was obtained when attempting to determine their charge, Figure S9). These gold cations are chelated by cyclooctene, when present in the electrolyte, before to grow into gold NPs.

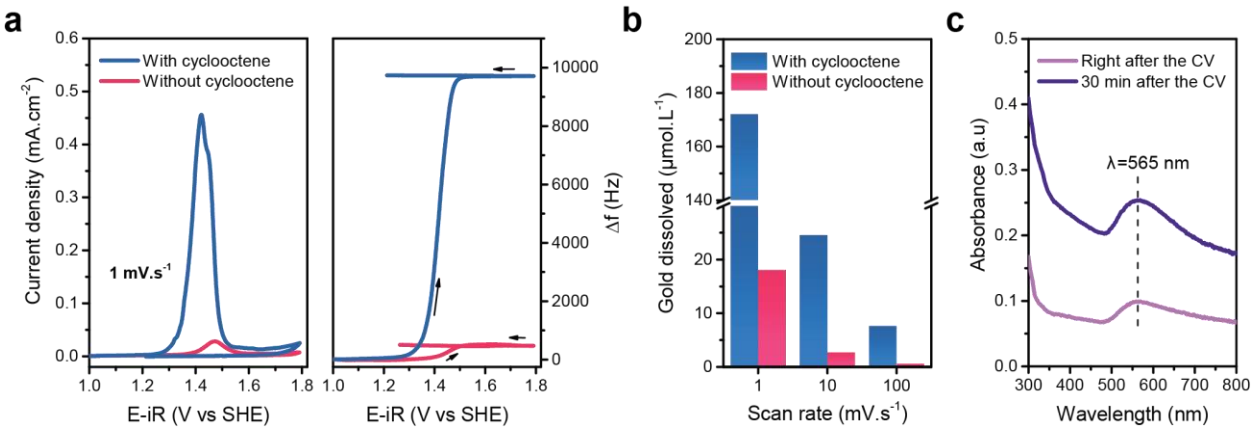

Figure 2. (a) CV obtained at EQCM electrodes and simultaneous frequency response in the absence of cyclooctene (red curves) and in the presence of cyclooctene (blue curves). WE: 9 MHz Au/Ti patterned quartz resonator, CE: Pt wire, Ref: leakless Ag/AgCl, Ar-saturated ACN/5 M water/0.1 M $TBAClO_4$/0 or 200 mM cyclooctene, 1 $mV.s^{-1}$, no stirring. (b) Quantity of gold dissolved into the electrolyte determined by ICP-MS upon cycling in the 1.0 – 1.8 V vs SHE window with and without cyclooctene as a function of scan rate. (c) Ex situ UV-Vis spectrum of the electrolyte right after (light purple) and 30 min after (dark purple) an anodic scan performed at 0.1 $mV.s^{-1}$ in the presence of cyclooctene. The CV was performed at 0.1 $mV.s^{-1}$ to allow for significant gold dissolution into the electrolyte. WE: polycrystalline gold, CE: Pt wire, Ref: leakless Ag/AgCl, Ar-saturated ACN/5 M water/0.1 M $TBAClO_4$/200 mM cyclooctene, 1,600 rpm.

Epoxidation mechanisms at gold electrodes. Two regions of interest well separated in potential thus exist for the electrochemistry of gold in ACN/water mixture. In the 1.2 – 1.7 V vs SHE region, metallic gold is substantially dissolved into the electrolyte before the passivation of the electrode by the formation of a gold oxide layer, whereas at more anodic potentials water is oxidized at gold oxide surfaces. We then took advantage of the existence of these two separate regions to study the epoxidation of cyclooctene at metallic gold and at gold oxide surfaces. Chronoamperometry measurements at potentials of interest were performed and the products formed analyzed by gas chromatography – mass spectrometry (GC-MS). To study the epoxidation of cyclooctene at the

surface of metallic gold, four potentials were selected (Figure 3a, the corresponding electrolysis curves are given in Figure S10). Figures 3a and b show that at potentials where substantial gold dissolution is happening (1 C passed at 1.40 and 1.46 V vs SHE), 36.3 and 56.5 µmol.L^{-1}.C^{-1} of cyclooctene oxide were produced, corresponding to Coulombic efficiencies (CEs) of 2.9 and 4.5% respectively (no overoxidation products such as cyclooctanone were detected). However, at 1.54 and 1.60 V vs SHE, potentials at which gold dissolution is negligible owing to the formation of a gold oxide layer, very low electrolysis currents were obtained and consequently, no epoxide or overoxidation products were detected by GC-MS. A chemical reaction between cyclooctene and oxygen ligands at the surface of the electrochemically generated oxide layer can thus be excluded to explain the formation of epoxide detected at lower potentials. These results point toward a sacrificial epoxidation mechanism in the corresponding potential range, where dissolved gold species play a critical role. It must be emphasized that electrolysis tests were performed using a rotating disk electrode (RDE) (0.196 cm^2 gold RDE immersed in 4 mL of electrolyte), explaining the relatively low CEs obtained. Using high surface area electrodes in electrochemical cells adapted to electrolysis would certainly help increasing the epoxidation CE, but given the low efficiency of gold as an epoxidation catalyst and the sacrificial nature of the mechanism at low potentials (see discussion below), no specific effort was paid toward optimization.

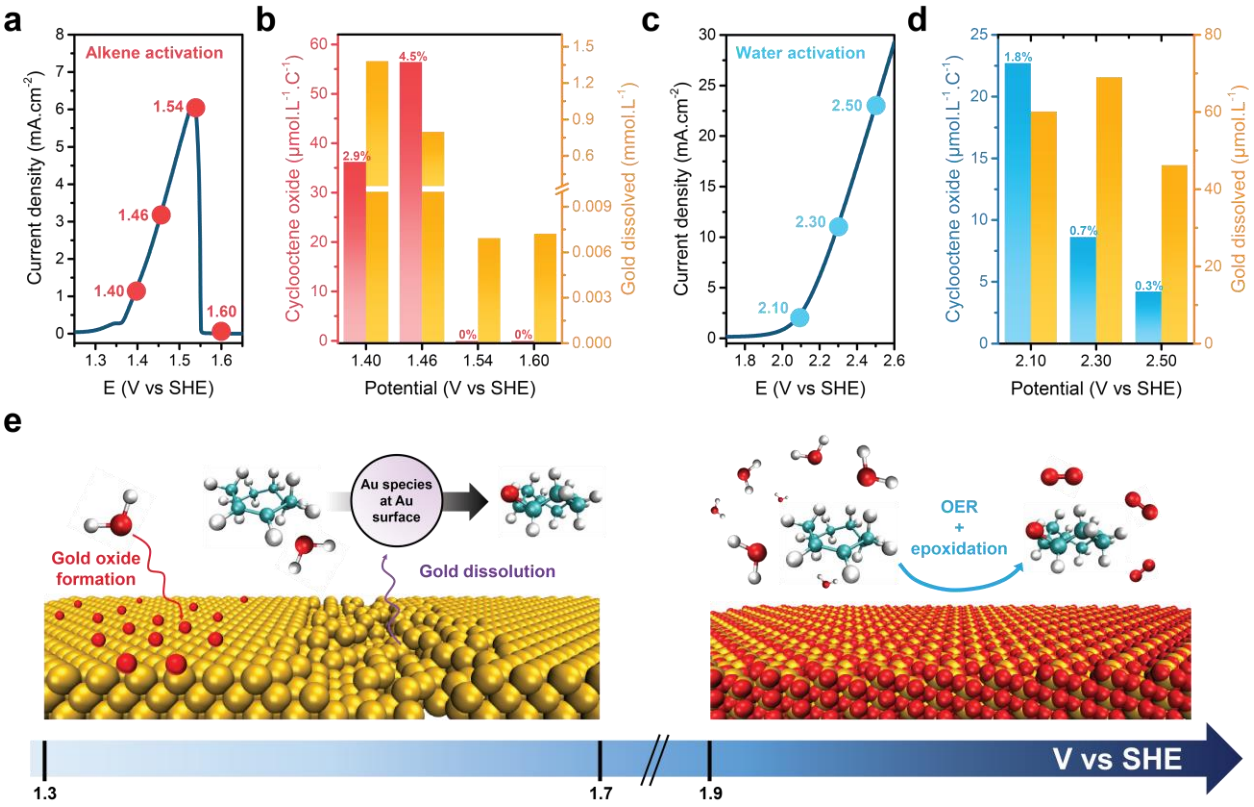

Figure 3. (a) Electrolysis potentials selected for the low overpotential mechanism (CV recorded at 0.1 $mV.s^{-1}$) and (b) corresponding cyclooctene oxide produced per volume of electrolyte and charge passed (the associated CE is given on top of the red bars) and quantity of gold dissolved during the electrolysis per volume of electrolyte. (c) Electrolysis potentials selected for the high overpotential mechanism and (d) corresponding cyclooctene oxide produced per volume of electrolyte and charge passed (the associated CE is given on top of the blue bars) and quantity of gold dissolved during the electrolysis per volume of electrolyte. (e) Simplified view of the two epoxidation mechanisms at gold electrodes depending on the potential range.

Homogeneous gold cationic complexes being known to π-activate alkenes toward nucleophilic attack,[68] it is likely that the epoxidation first proceeds by the activation of the substrate, cyclooctene, by dissolved cationic gold species at the surface of gold, which then react with water. The epoxide is finally formed following the transfer of hydrogen atoms. A simplified view of the epoxidation mechanism and the redox processes involved is given on the left panel of Figure 3e. However, the lifetime of these gold cationic species is certainly very short, as discussed above for the UV-Vis results, and attempts to catalyze the oxidation of cyclooctene by first dissolving gold

from metallic electrodes were unsuccessful, reinforcing our conclusion that cationic species are the ones predominantly responsible for the activation of cyclooctene (Figure S11).

To study the epoxidation of cyclooctene at gold oxide surfaces, electrolysis tests were performed at three potentials (Figure 3c, corresponding electrolysis curves are given in Figure S12). Cyclooctene oxide was detected for the three potentials, with quantities and CEs lower than those obtained at gold metallic surfaces (Figure 3d), indicating that at these very high potentials, overoxidation is not negligible (7.8, 1.8 and 0.9 $\mu mol.L^{-1}.C^{-1}$ of cyclooctanone were detected after electrolysis at 2.1, 2.3 and 2.5 V vs SHE respectively). Interestingly, the CE toward epoxidation decreases when the applied potential increases, showing that at higher voltages the OER is favored. The amount of gold dissolved relative to the charge passed is two orders of magnitude lower than that for the previous mechanism, showing that at these potentials, gold dissolution is minimal and that the mechanism is not sacrificial (Figure S13). More striking is the observation that the catalytic current recorded in the OER potential range is identical with or without cyclooctene (Figure 1a). Such similarity, previously observed in the literature but not discussed,[27,29] suggest that the OER and the epoxidation may share similar intermediates, as schematically represented on the right panel of Figure 3e. Considering the steps commonly accepted for the OER, water adsorption $H_2O + * = *OH + H^+ + e^-$ followed by a deprotonation step $*OH = *O + H^+ + e^-$ (* denotes a surface site) may be shared between the OER and the epoxidation. On the contrary, the O-O bond formation step $*O + H_2O = *OOH + H^+ + e^-$ and the final oxygen evolution $*OOH = * + O_2 + H^+ + e^-$ are unique to the OER. Observing that the CE for epoxidation decreases with overpotential, kinetic control of the epoxidation reaction may originate from a step that differs from the O-O bond formation or oxygen evolution ones and that potentially does not involve electron transfer, such as the reaction of the alkene with surface *O species.

These results thus reveal that two epoxidation mechanisms are at play on the surface of gold electrodes in ACN/water mixtures, depending on the potential range. These two mechanisms, driven by different chemistries at the surface of gold, differ in nature, with one on the surface of metal oxides being heterogeneous and sharing common intermediates with the OER, i.e. water activation, while the other one most likely follows the activation of the substrate, cyclooctene, by the *in situ* formation of an homogeneous cationic metal catalyst. However, for the latter mechanism, the role of gold NPs and surface roughness caused by dissolution on the epoxidation reaction cannot be overruled. Gaining more insight into the species involved would require a comprehensive study on its own.

Effect of the nature of the supporting salt cation. Previous studies have revealed that the nature of the supporting salt cation can change the hydrophilicity of the electrochemical double layer, thus allowing for tuning the kinetics and selectivity of electrochemical reactions.[50,57,58] Our attention then turned to the effect of supporting salt cations on the epoxidation mechanisms at low and high potentials, where cyclooctene and water are activated, respectively. Three cations were selected, one organic and hydrophobic cation (TBA^+) and two inorganic ones (Li^+ and Na^+) having different Lewis acidities. Figures 4a and b show that the catalytic current corresponding to water activation at high potentials is not affected by the nature of the cation. This result is in line with previous studies showing that cations only influence the kinetics of the best performing catalysts for the OER and HER, i.e. those requiring lower driving force.[69,70] At lower potentials, the electrochemical response in Li^+- and Na^+-containing electrolytes is found to be similar, pinpointing that for hydrophilic cations, the strength of the short-range cation-water interaction (stronger for Li^+ than for Na^+) does not affect the dissolution of gold and the formation of gold oxide (Figure 4a). In the presence of cyclooctene (Figure 4b), the anodic charge Q_{ox} at 10 $mV.s^{-1}$ is significantly

greater (~ 30 times) with the hydrophobic cation TBA^+ than that recorded for the two inorganic cations, whereas only a slight increase is observed without cyclooctene (~ 2 times).

As similar electrochemical responses are recorded for Li^+ and Na^+ independently of the presence of cyclooctene, we then restricted the comparison to TBA^+ and Li^+ in the following. EQCM measurements show that the increased charge passed with TBA^+ compared to Li^+ independently of the presence of cyclooctene is correlated to an increase in frequency of the quartz resonator of the same order of magnitude (Figure S14). The EQCM responses thus show that the dissolution of gold in TBA^+-containing electrolytes is more important than in Li^+-containing ones (higher frequency increase for an anodic scan in TBA^+-containing electrolytes) and therefore reveal that the nature of the supporting salt cation mainly affects gold dissolution into the electrolyte. As a consequence of the greater amount of dissolved gold species, electrolysis performed at 1.46 V vs SHE shows that more epoxide is produced in the TBA^+-containing electrolyte compared to the Li^+-containing one (Figure 4c). Quantitatively, ~ 8.5 times more gold is dissolved during electrolysis with the TBA^+-containing electrolyte whereas the associated CE is only two times higher, highlighting again the poor catalytic efficiency of dissolved gold species toward epoxidation. For the mechanism at high potentials, as expected, since no difference is observed

between the different cations (Figure 4b), the amount of cyclooctene oxide produced during electrolysis at 2.30 V vs SHE in TBA^+- and Li^+-containing electrolytes is similar (Figure 4d).

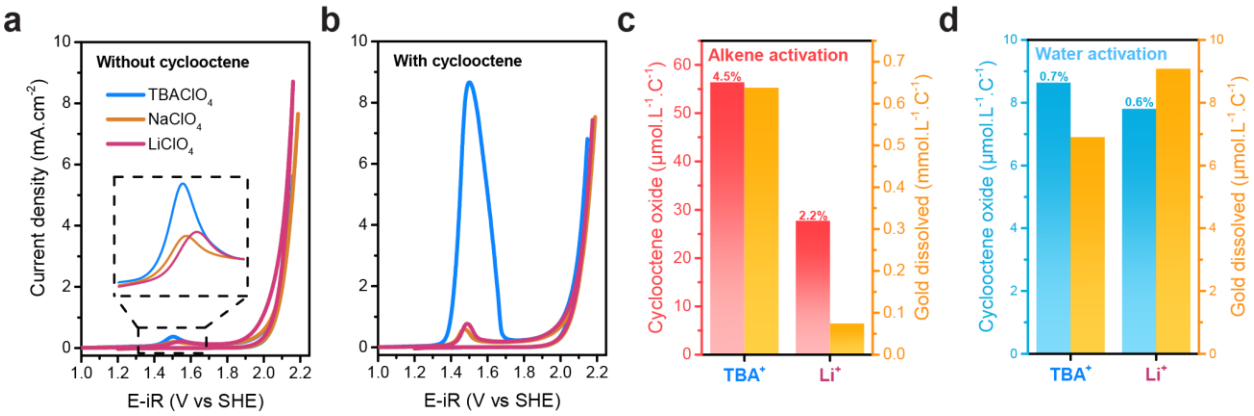

Figure 4. Cyclic voltammograms obtained at a rotating gold electrode in ACN/water mixture (a) in the absence and (b) in the presence of cyclooctene as a function of the supporting salt cation (TBA^+: blue, Na^+: orange and Li^+: mauve). WE: polycrystalline gold, CE: Pt wire, Ref: leakless Ag/AgCl, Ar-saturated ACN/5 M water/0.1 M $TBAClO_4$ or $NaClO_4$ or $LiClO_4$/0 or 200 mM cyclooctene, 10 $mV.s^{-1}$, 1,600 rpm. (c) Quantity of cyclooctene oxide and gold dissolved during electrolysis at 1.46 V vs SHE for the TBA^+- and Li^+-containing electrolytes and (d) quantity of cyclooctene oxide and gold dissolved during electrolysis at 2.3 V vs SHE for the TBA^+- and Li^+-containing electrolytes.

To rationalize the experimental results gathered at low potentials, classical molecular dynamics (MD) simulations were first performed for TBA^+- and Li^+-containing bulk electrolytes (full details on the simulations are given in the Methods and the composition of the simulation boxes is given in Tables S1 and S2). The existence of aqueous and organic domains at the nanoscale in ACN/water (10 wt% water) was demonstrated in a previous study.[50] Adding cyclooctene in ACN/5 M water (corresponding to ~ 11 wt% water) mixtures does not alter the nanostructuring of the electrolyte, which is visible on snapshots shown in Figure 5a and b. Analysis of the simulations shows that, as expected, cyclooctene is located in the organic nanodomains (Figure S15) and that the presence of cyclooctene in the electrolyte does not disturb the aqueous nanodomains (Figure S16). Bulk MD simulations show that in both TBA^+- and Li^+-containing electrolytes, cyclooctene is solvated by the same number of ACN and water molecules (Figure S15). Although a slight

preferential interaction between cyclooctene and TBA^+ terminal carbons exists (Figure 5c, top), the non-polarizability of cyclooctene prevents any favorable interaction with any cation (Figure 5c, bottom). The solvation shell of cyclooctene is thus the same in both electrolytes. Therefore, no difference in bulk solvation structure can explain the aforementioned experimental results.

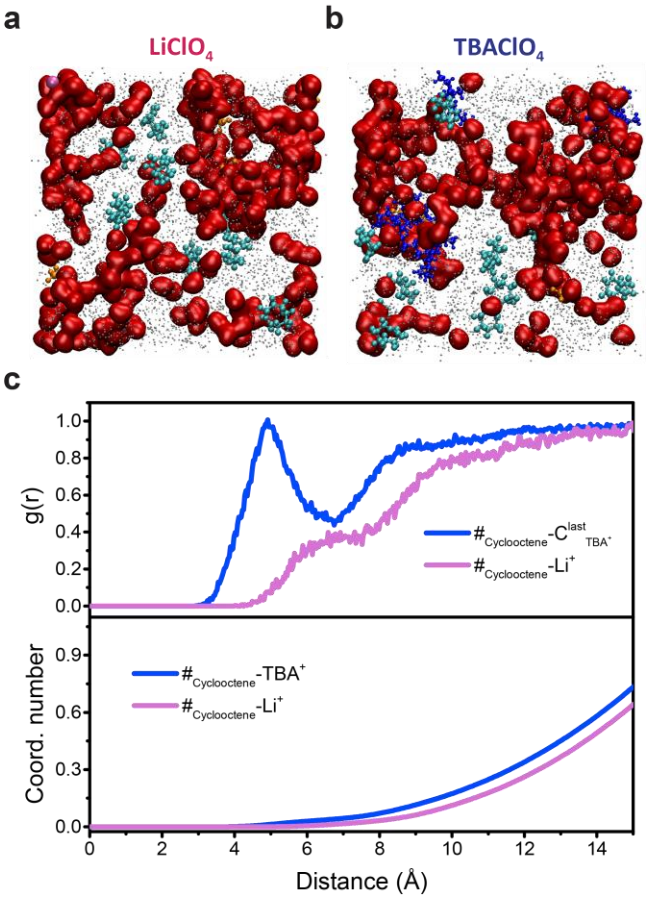

Figure 5. Snapshots of the bulk MD simulations in (a) Li^+- and (b) TBA^+-containing electrolytes in the presence of cyclooctene. Water molecules are represented in red, ACN in grey (the size of which was decreased for clarity), ClO_4^- in orange, TBA^+ in deep blue, Li^+ in mauve and cyclooctene in cyan. (c) Top: radial distribution function, g(r), between cyclooctene's center of mass (#) and the terminal carbons of TBA^+ (blue) and Li^+ (purple). Down: number of TBA^+ and Li^+ surrounding cyclooctene as computed from the corresponding g(r)'s.

We then focused on the structure of the electrochemical double layer at the anode as a function of the supporting salt cation. For that, classical MD simulations at electrified interfaces applying a constant voltage of 1V between two planar gold electrodes were performed for TBA^+- and Li^+-

containing electrolytes in the presence and in the absence of cyclooctene (full details on the simulations are given in the Methods and the composition of the simulation boxes is given in Tables S3 and S4). Snapshots of the simulations in the absence of cyclooctene (Figure 6a) and corresponding density profiles of water and ACN in the vicinity of the electrode (Figure 6b and c) show that water adsorption at the surface of gold is very low compared to that of ACN in both electrolytes, a phenomenon already observed in the literature for Pt surfaces.[71] As seen on the density profile of water (Figure 6b), the interface is more hydrophilic in the presence of Li^+ cations than in the presence of hydrophobic TBA^+ cations whereas no difference is found between both electrolytes for the adsorption of ACN (Figure 6c). It is noteworthy that Li^+ cations are adsorbed on the anode (Figure 6a and Figure S17), the strength of which will be discussed below. The Li^+-OH_2 interaction being strong (Figure S18), the adsorbed Li^+ brings water molecules to the surface, explaining the more hydrophilic interface found for the Li^+-containing electrolyte. In the presence of cyclooctene, water adsorption is also very low compared to that of ACN and cyclooctene is found to favorably adsorb at the gold electrode, contributing to the increase of the hydrophobicity of the interface for both Li^+ and TBA^+ (Figure 6d and S19). Nevertheless, for the electrolyte containing Li^+ cations, the interface retains some hydrophilicity due to the presence of Li^+ cations adsorbed at the anode which, as discussed without cyclooctene, helps bringing water at the interface.

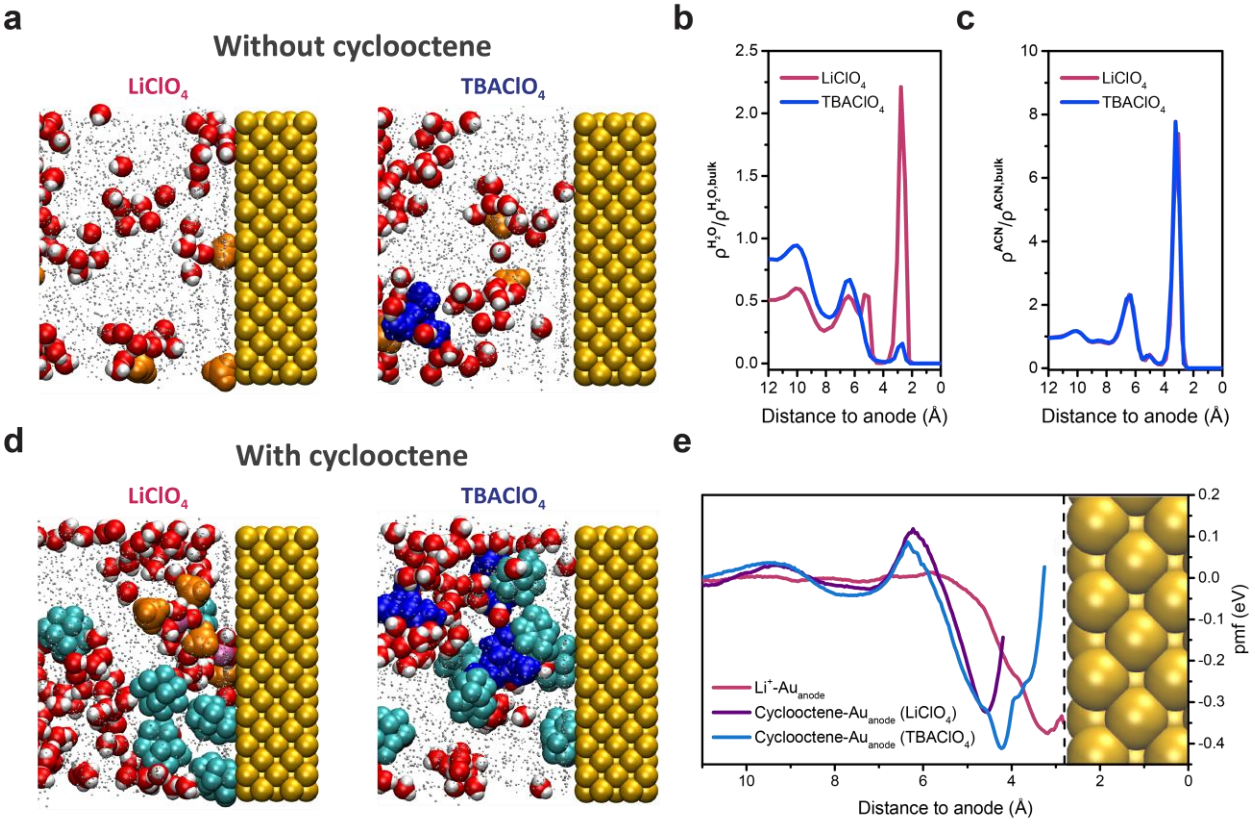

Figure 6. (a) Snapshots of the MD simulations at electrified interfaces in the vicinity of the gold anode in the absence of cyclooctene in Li^+- and TBA^+-containing electrolytes. Density profiles of (b) water and (c) ACN at the anode interface in Li^+- (mauve) and TBA^+-containing (blue) electrolytes in the absence of cyclooctene. (d) Snapshots of the MD simulations at electrified interfaces in the vicinity of the gold anode in the presence of cyclooctene in Li^+- and TBA^+-containing electrolytes. (e) Potentials of mean force (pmf) between Li^+ (mauve), cyclooctene's center of mass in Li^+-containing electrolyte (purple), cyclooctene's center of mass in TBA^+-containing electrolyte (blue) and gold anode atoms as obtained from umbrella sampling calculations. For the snapshots, oxygen and hydrogen atoms of water molecules are represented in red and white respectively, ACN in grey (the size of which was decreased for clarity), ClO_4^- in orange, TBA^+ in deep blue, Li^+ in mauve and cyclooctene in cyan. For the density profiles and the pmf, the distance to the anode refers to the distance to the center of mass of the gold atoms constituting the first layer of the anode, i.e. the ones in contact with the electrolyte.

As the adsorption of Li^+ and cyclooctene molecules at the anode found from the MD simulations drastically affects the structure of the electrochemical double layer and particularly its hydrophilicity, the strength of their adsorption was quantified before drawing further conclusions. However, the relatively low number of Li^+ and cyclooctene molecules in the simulation boxes (20 and 40 respectively) prevents the sampling of the density profiles to derive any potential of mean

force (pmf) between these species and gold atoms of the electrode. To circumvent this limitation, pmf were obtained using the umbrella sampling technique,[72] which allows for the sampling of the adsorption profiles of Li^+ and cyclooctene molecules at the anode/electrolyte interface (see Methods). The umbrella sampling technique was used for the systems with electrolytes containing cyclooctene and the obtained pmf shown in Figure 6e confirm the strong adsorption of Li^+ and cyclooctene at the gold anode (a discussion on the shape of cyclooctene adsorption profiles in both electrolytes is given in Figure S20). Indeed, adsorption free energies of -387, -442, and -498 meV were obtained for Li^+, cyclooctene in the Li^+- and in the TBA^+-containing electrolyte, respectively, more than two times higher than the free energy associated to the Li^+-OH_2 interaction in the bulk (Figure S18).

The experimental results gathered at low potentials can therefore be explained by a change in the hydrophilicity of the electrode/electrolyte interface as a function of the supporting salt cation. In the absence of cyclooctene, the favorable adsorption of Li^+ cations at the gold anode brings water molecules to the surface and consequently increases the hydrophilicity of the interface. The increased hydrophilicity of the interface thus favors the reactivity of water toward the formation of gold oxide over gold dissolution, which explains the higher gold dissolution observed in the TBA^+-containing electrolyte as compared to the Li^+-containing one (Figure 4a and S14a). In the presence of cyclooctene, two phenomena are at stake. The favorable adsorption of cyclooctene molecules at the anode in both electrolytes contributes to making a more hydrophobic interface in both cases. However, in the presence of Li^+ cations, there is a competition between the adsorption of Li^+ and that of cyclooctene owing to adsorption free energies of the same order of magnitude, thus providing a means for water to access the surface. As a consequence, in the presence of cyclooctene, the gold oxide formation is also favored over gold dissolution in the presence of Li^+

cations. Bearing in mind that the chelating power of cyclooctene drastically increases gold dissolution into the electrolyte, the consequences of having a more hydrophobic interface in the TBA^+-containing electrolyte are amplified, explaining the much greater gold dissolution observed as compared to the Li^+-containing one in the presence of cyclooctene (Figure 4b and S14b). More importantly for the application, the greater amount of dissolved gold species in the presence of TBA^+ cations as compared to Li^+ cations results in an improved epoxidation yield (Figure 4c). Our results thus show that tuning the hydrophilicity/hydrophobicity of the electrochemical interface can modulate the selectivity of complex anodic reactions.

CONCLUSION

In summary, through a careful selection of electrocatalyst and electrolyte composition, we have demonstrated that epoxidation mechanisms are drastically dependent on the surface of the electrocatalyst. By exploiting the fact that in ACN/water mixtures water reactivity at gold metallic surfaces is decoupled from that at gold oxide surfaces, we have gained insight into the role played by these two electrocatalytic surfaces on the transfer of oxygen from water to alkenes. This distinctive property allowed us to show that at metallic gold surfaces, the epoxidation of cyclooctene proceeds via the activation of the substrate by the *in situ* formation of an homogeneous cationic metal catalyst in a sacrificial manner whereas at gold oxide surfaces, the epoxidation mechanism shares similar reaction intermediates with the OER, i.e. water activation. Furthermore, we show that the mechanism at low overpotentials, i.e. the one at metallic gold, is strongly impacted by the electrolyte composition when changing the nature of the supporting salt cation, resulting from a modification of the hydrophilicity of the electrode/electrolyte interface. The electrode/electrolyte interface was shown to be more hydrophobic in the presence of TBA^+ cations as compared to Li^+ cations, resulting in an increased gold dissolution into the electrolyte and an

improved epoxidation Coulombic efficiency at gold metallic surfaces. However, due to the very high potentials required to activate water at gold oxides surfaces, the epoxidation mechanism at gold oxide was shown to be cation-independent. Anticipating transition metal oxides electrocatalysts capable of transferring oxygen atoms to organic molecules at lower potentials we can postulate that such cation-dependent mechanisms could be at stake, which would expand the scope of the present study. The effect of the nature of anions on anodic reactions such as epoxidation, which intuitively could be more pronounced than that of cations, is currently under investigation and could enrich the tuning of the electrode/electrolyte interface toward improved yield and selectivity. Finally, our study highlights that the mechanistic investigations of complex electrosynthetic reactions could benefit from the methodologies and knowledge gathered in the past few years in the electrocatalysis field, as recently suggested in the literature.[73]

METHODS

Reagents. Acetonitrile (99.9%, AcroSeal) was purchased from Acros Organics. Cis-cyclooctene (95%, stabilized with 100-200 ppm Irganox® 1076 FD), lithium perchlorate (anhydrous, 99%), sodium perchlorate (anhydrous, ACS, 98.0-102.0%) and tetra-n-butylammonium perchlorate (electrochemical grade) were purchased from Alfa Aesar. Anisole (anhydrous, 99.7%), cyclooctene oxide (99%), ferrocene (98%) and gold standard for ICP-MS (TraceCERT®, 1.000 ± 0.003 $mg.L^{-1}$ in 5% HCl) were purchased from Sigma-Aldrich. 1,5-cyclooctadiene (99+%, stabilized, purified by redistillation) was purchased from Fisher Scientific. Milli-Q® water (18.2 MΩ.cm at 25°C) was used for electrolytes containing water. Cyclooctene was kept in a fridge and regularly purged with argon to avoid any unwanted reaction with oxygen. Cyclooctene purity was regularly checked with ^{1}H-NMR and GC-MS.

Electrochemical measurements (general). Data were acquired on a BioLogic VSP potentiostat. All electrochemical measurements were recorded using a three-electrode cell setup with a leakless Ag/AgCl (ET069, diam. 5 mm, L 100 mm, eDAQ, provided by Mengel Engineering) reference electrode (regularly calibrated against ferrocene). A flame-annealed platinum wire or a graphite rod (L 150 mm, diam. 3 mm, low density, 99.995 % trace metals basis, Sigma-Aldrich) were used as a counter electrode and placed in a separate compartment. Prior to any measurement, glassy carbon, polycrystalline gold and polycrystalline platinum electrodes (5 mm diameter, 0.196 cm^2 geometric surface area, Pine research) were polished with three polishing slurries (6 µm diamond on nylon polishing disc, followed by 0.3 µm and 0.04 µm aluminum oxide on micro-cloth polishing disc) using a polishing machine (Le Cube, Presi). Residual traces of slurries were removed by sonicating the as-polished electrodes three times in water (1 min each) and one time in acetone (1 min). The ohmic drop was measured by electrochemical impedance spectroscopy

(EIS) after electrochemical measurements. Typical values of around 50 to 70 Ω were obtained. The ohmic drop compensation was performed manually during the data treatment (85% of correction). To remove metallic impurities, the cell and the separate compartment for the counter electrode were regularly washed with aqua regia and to remove organic impurities they were regularly washed with $KMnO_4/H_2SO_4$ (1 $g.L^{-1}$ $KMnO_4$ dissolved in 0.5 M H_2SO_4) solution followed by a diluted 1:1 H_2O_2/H_2SO_4 solution.

Preparation of electrolyte solutions. Solutions of 0.11 M supporting salt (lithium, sodium and tetra-n-butylammonium perchlorate) in acetonitrile were prepared by dissolving respectively 585.2, 673.4 and 1,880.5 mg of the corresponding salt in 50 mL of dry acetonitrile. The electrolytes that do not contain any organic substrate were prepared as follow: the 0.11 M supporting salt acetonitrile solutions were mixed with 0.90 mL of Milli-Q® water in a 10 mL volumetric flask to give acetonitrile/water mixtures containing 0.10 M supporting salt and 5.0 M water. The final concentration of supporting salt was calculated after experimentally measuring the density of the 0.11 M supporting salt acetonitrile solutions (0.789 $g.cm^{-3}$ at room temperature, no significant difference was observed with the different supporting salts) and the density of the final acetonitrile/water mixture (cf. Table S1 and S2). The electrolytes containing 200 mM cyclooctene were prepared as follow: the 0.11 M supporting salt acetonitrile solutions were mixed with 0.92 mL of Milli-Q® water in a 10 mL volumetric flask. Then, 4.0 mL of this mixture were degassed with Ar and mixed with 114 µL of cyclooctene right before the electrochemical experiments giving a mixture containing 0.098 M supporting salt, 4.98 M water and 200 mM cyclooctene.

Electrochemical Quartz Crystal Microbalance experiments (EQCM).

EQCM measurements were conducted using a lab-made microbalance setup connected to a Biologic potentiostat (SP200). Gold patterned quartz resonators (with polished surface finish) were

used as working electrodes (Ti/Au coated QCM sensor operating at 9 MHz, 14 mm diameter, gold electrode surface of 0.2 cm^2, AWSensors, Valencia, Spain) in Ar-saturated ACN/5 M water/0.1 M TBA or $LiClO_4$/0 or 200 mM cyclooctene and in 0.1 M $HClO_4$. A Pt wire (placed in a separate compartment) and a leakless Ag/AgCl were used as counter and reference electrodes, respectively.

Gas chromatography – mass spectrometry measurements (GC-MS).

Products generated by electrolysis were analyzed and quantified by GC-MS on a Shimadzu GCMS-QP2020 equipped with a polar Restek SH-Rtx-Wax column (59.7m x 0.32mm x 0.50µm). Anisole was used as an internal standard for each sample. After each electrolysis, 980 µL of electrolyte were mixed with 20 µL of a 0.10 M anisole solution in acetonitrile. 0.5 µL of the as-prepared mixtures were injected into the GC-MS machine. The parameters used for the gas column and the mass spectrometer were:

- GC: injection mode: Split with a ratio of 20.0, column oven temperature: 70°C, final temperature: 240°C, heating rate: 10°C/min, holding time at 240°C: 5 min.
- MS: ion source temperature: 200°C, acquisition mass range: 12-200 m/z, scan speed: 5000 $amu.s^{-1}$.

A cutoff of 5 min was applied to avoid saturating the detector with acetonitrile and cyclooctene. Anisole retention time was ~ 8.2 min and cyclooctene oxide retention time was ~ 10.2 min. The limit of detection for cyclooctene oxide was estimated to be 0.01 mM by injecting samples with varying known concentrations of cyclooctene oxide.

Inductively coupled plasma mass spectrometry (ICP-MS).

ICP-MS measurements were performed on a PerkinElmer NexION 2000 ICP mass spectrometer equipped with an autosampler (flash sample: 80s, peristaltic pump speed: 42 rpm). Prior to

measurements, the instrument was calibrated and the performance check was performed using PerkinElmer's NexION setup solution (TruQ™ms, 1 µg.L^{-1} Be, Ce, Fe, In, Li, Mg, Pb, U in 1% HNO_3). For each set of measurements, a standard range of 0.05; 0.10; 1.0; 10 and 100 ppb Au solutions in 2.0 wt% HNO_3 in Milli-Q® water was prepared using the gold standard solution for ICP-MS (TraceCERT®, 1.000 ± 0.003 mg.L^{-1} in 5% HCl). Each set of measurement was performed following the same procedure:

1) Measurement of 2 blank samples (2 wt% HNO_3 in Milli-Q® water)
2) Measurement of samples belonging to the standard range
3) Measurement of 2 blank samples (2 wt% HNO_3 in Milli-Q® water)
4) Measurement of 1 "verification sample" at 1 ppb of the desired element
5) Measurement of 1 blank sample (2 wt% HNO_3 in Milli-Q® water)
6) Measurement of samples of interest (if the number of samples to measure was greater than 15, one blank sample, one "verification sample" and another blank sample were measured after the 15^{th} sample).

After each electrochemical experiment, the electrolyte was collected in a vial and 5 mL of 2.0 wt% HNO_3 solution in Milli-Q® water were poured into the electrochemical cell to collect the remaining gold. To prepare the ICP samples, 250 µL of the collected electrolyte and 250 µL of the 5mL of the 2.0 wt% HNO_3 washing solution were added in two separate 25 mL volumetric flasks which were completed by 2.0 wt% HNO_3 solution. When an ICP sample was too concentrated and exceeded the upper limit of the standard range it was diluted again by 100. The cell and the separate compartment for the counter electrode used for the electrochemical experiments were washed with aqua regia after each experiment to remove any remaining traces of gold.

UV-vis spectroscopy.

UV-vis spectra were recorded on a Mettler Toledo UV5bio spectrometer.

Bulk molecular dynamics simulations.

Classical MD simulations of the bulk electrolytes were performed using the MetalWalls code.[74] Acetonitrile solvent was described with a six-site model.[75] The SPC/E model was chosen for water molecules.[76] Force field parameters for perchlorate anions and TBA cations were taken from ref. 77 and ref. 78 respectively. OPLS-AA force field was chosen for cyclooctene and was generated by Aten molecular modelling software (v1.9). The Lennard–Jones parameters for Li^+ were taken from Åqvist.[79] Mixed Lennard–Jones parameters for all of the different atom types were obtained using the Lorentz–Berthelot combination rules. The simulations were performed in the NVT ensemble at 298 K for 60 ns using the Nosé-Hoover thermostat[80,81] (relaxation time of 0.5 ps) with a timestep of 1 fs and saving configurations every 1 ps. The number of each molecule/atom in the boxes (the number of $LiClO_4$ or $TBAClO_4$ was fixed to 5 per box) and the size of the boxes were calculated to match the experimental densities of the investigated electrolytes (the physical properties of the different electrolytes and the corresponding box configurations are given in Tables S1 and S2). The initial configuration was obtained by generating a cubic box using the PACKMOL package.[82] Long-range electrostatic interactions were computed with the Ewald summation method, while a cut-off of 9 Å was adopted for the non-bonded interactions. The SHAKE algorithm was employed to constrain the stretching interactions involving hydrogen atoms.[83,84] All the analyses were performed on the last 50 ns with TRAVIS[85,86] and VMD software was used to visualize boxes and generate snapshots.[87]

Molecular dynamics simulations at constant applied voltage.

Classical MD simulations of the electrolytes at the interface with gold electrodes at constant applied voltage were also performed using the MetalWalls code.[74] The same force fields for the electrolyte molecules as for the bulk simulations were used. The simulations were performed at a fixed potential difference of 1V between two planar gold electrodes following the approach detailed in refs. 88,89. Each gold electrode had a size of 36.63 x 36.63 Å and was made of 810 gold atoms arranged in 5 slabs of 162 atoms each ((100) orientation). The Lennard-Jones parameters for the electrode gold atoms were taken from ref. 90. 2D periodic boundary conditions were used in the *xy* directions. The simulations were performed in the NVT ensemble at 298 K with the Nosé–Hoover thermostat[80,81] (relaxation time constant of 0.5 ps) using a timestep of 1 fs and saving configurations every 1 ps. Long-range electrostatic interactions were computed with the Ewald summation method in 2D with a combination of point charges for the electrolyte and Gaussian charges for the electrodes,[88,91] the latter with a Gaussian width taken from ref. 92, while a cut-off distance of 12 Å was adopted for the non-bonded interactions. The SHAKE algorithm was employed to constrain the stretching interactions involving hydrogen atoms.[83,84] The number of electrolyte atoms/molecules used was increased fourfold as compared to boxes for bulk simulations (boxes configurations are given in Tables S3 and S4). In order to obtain the correct liquid density, the electrodes were allowed to move in the *z* direction, by applying a pressure on both side with the help of a piston, and simulations were performed until the electrodes oscillate around an equilibrium value (this step taking 1 to 2 ns depending of the system). Then, the pistons were removed (the *z* dimensions given in Tables S3 and S4 correspond to the size in the *z* direction of the boxes after the pistons were removed) and the systems were simulated for another 0.5 ns to ensure that the density at the center of the box matches the density of the bulk. Finally, a constant potential difference of 1V was applied between the two electrodes, and the systems were simulated

until the electrode charges equilibrated (5 to 10 ns depending on the system), followed by a production run of 5 ns. VMD software was used to visualize boxes and generate snapshots.[87] The umbrella sampling calculations of Li^+ and cyclooctene adsorption profiles along the *z* coordinate was accomplished using the open-source PLUMED library, version 2.7.1.[93] For both species, nine calculations were performed at *z* values of 1.0, 2.0, 3.0, 4.0, 5.0, 6.0, 7.0, 8.0 and 9.0 Å from the anode surface with a spring constant of 2,500 $kJ.mol^{-1}.nm^{-2}$.

ASSOCIATED CONTENT

Additional experimental (cyclic voltammetry, rotating ring disk electrode measurements, electrolysis curves, EQCM, ICP-MS) and MD simulations data to support the results of the main text (Figures S1-S20, Tables S1 to S4).

AUTHOR INFORMATION

Corresponding Author

Alexis Grimaud – Department of Chemistry, Merkert Chemistry Center, Boston College, Chestnut Hill, MA; Chimie du Solide et de l'Energie, UMR 8260, Collège de France, 75231 Paris Cedex 05, France ; Réseau sur le stockage Electrochimique de l'Energie (RS2E), CNRS FR3459, 80039 Amiens Cedex, France ; https://orcid.org/0000-0002-9966-205X; Email: alexis.grimaud@bc.edu

Authors

Florian Dorchies – Chimie du Solide et de l'Energie, UMR 8260, Collège de France, 75231 Paris Cedex 05, France; Sorbonne Université, France; Réseau sur le stockage Electrochimique de l'Energie (RS2E), CNRS FR3459, 80039 Amiens Cedex, France ; https://orcid.org/0000-0003-2300-7582

Alessandra Serva – Réseau sur le stockage Electrochimique de l'Energie (RS2E), CNRS FR3459, 80039 Amiens Cedex, France; Sorbonne Université, CNRS, Physicochimie des Électrolytes et

Nanosystèmes Interfaciaux, PHENIX, F-75005 Paris, France; https://orcid.org/0000-0002-7525-2494

Dorian Crevel – Réseau sur le stockage Electrochimique de l'Energie (RS2E), CNRS FR3459, 80039 Amiens Cedex, France; Université Paris-Saclay, Univ Evry, CNRS, LAMBE, 91025, Evry-Courcouronnes, France; https://orcid.org/0000-0003-4808-4429

Jérémy De Freitas – Laboratoire d'Electrochimie Moléculaire, Université de Paris, CNRS, F-75006 Paris, France

Nikolaos Kostopoulos – Laboratoire d'Electrochimie Moléculaire, Université de Paris, CNRS, F-75006 Paris, France; https://orcid.org/0000-0001-9500-9662

Marc Robert – Laboratoire d'Electrochimie Moléculaire, Université de Paris, CNRS, F-75006 Paris, France; Institut Universitaire de France (IUF), 75231 Paris, France; https://orcid.org/0000-0001-7042-4106

Ozlem Sel – Chimie du Solide et de l'Energie, UMR 8260, Collège de France, 75231 Paris Cedex 05, France; Réseau sur le stockage Electrochimique de l'Energie (RS2E), CNRS FR3459, 80039 Amiens Cedex, France ; https://orcid.org/0000-0002-8501-4561

Mathieu Salanne – Réseau sur le stockage Electrochimique de l'Energie (RS2E), CNRS FR3459, 80039 Amiens Cedex, France; Sorbonne Université, CNRS, Physicochimie des Électrolytes et Nanosystèmes Interfaciaux, PHENIX, F-75005 Paris, France; Institut Universitaire de France (IUF), 75231 Paris, France; https://orcid.org/0000-0002-1753-491X

AUTHORS CONTRIBUTION

F.D and A.G conceived the idea and designed the experiments. F.D prepared the electrolytes and carried out all the electrochemical experiments. O.S prepared the EQCM electrodes and F.D carried out the EQCM experiments with the help of O.S. N.K designed the GC-MS procedure, F.D prepared the GC-MS samples and measured them together with J.D.F and N.K. The ICP-MS procedure was designed by D.C, the samples prepared by F.D and measured by D.C. F.D performed the classical bulk MD simulations and MD simulations at electrified interfaces under the guidance of A.S and the simulations were analyzed and designed together with A.S and M.S. All the authors edited the manuscript and discussed the scientific results.

ACKNOWLEDGEMENTS

F.D thanks the École normale supérieure Paris-Saclay for his PhD scholarship. The authors acknowledge HPC resources granted by GENCI (resources of IDRIS, Grant No. A0120910463) and by the SACADO service unit of Sorbonne University. This work was funded by the European Research Council (ERC) under the European Union's Horizon 2020 research and innovation program (grant agreement 771294). The authors thank Roxanne Berthin for help with the molecular dynamics simulations.

Notes

The authors declare no competing interests.

REFERENCES

(1) Frontana-uribe, B. A.; Little, R. D.; Ibanez, J. G.; Vasquez-medrano, R. Organic Electrosynthesis : A Promising Green Methodology in Organic Chemistry. *Green Chem.* **2010**, *12*, 2099–2119. https://doi.org/10.1039/c0gc00382d.

(2) Horn, E. J.; Rosen, B. R.; Baran, P. S. Synthetic Organic Electrochemistry: An Enabling and Innately Sustainable Method. *ACS Cent. Sci.* **2016**, *2* (5), 302–308. https://doi.org/10.1021/acscentsci.6b00091.

(3) Jing, Q.; Moeller, K. D. From Molecules to Molecular Surfaces. Exploiting the Interplay between Organic Synthesis and Electrochemistry. *Acc. Chem. Res.* **2020**, *53* (1), 135–143. https://doi.org/10.1021/acs.accounts.9b00578.

(4) Zhu, C.; Ang, N. W. J.; Meyer, T. H.; Qiu, Y.; Ackermann, L. Organic Electrochemistry: Molecular Syntheses with Potential. *ACS Cent. Sci.* **2021**, *7* (3), 415–431. https://doi.org/10.1021/acscentsci.0c01532.

(5) Hammerich, O.; Speiser, B. *Organic Electrochemistry. Revised and Expanded*, 5th ed.; CRC Press: Boca Raton, FL, USA, 2015. https://doi.org/10.1201/b19122.

(6) Yan, M.; Kawamata, Y.; Baran, P. S. Synthetic Organic Electrochemical Methods Since 2000 : On the Verge of a Renaissance. *Chem. Rev.* **2017**, *117* (21), 13230–13319. https://doi.org/10.1021/acs.chemrev.7b00397.

(7) Shatskiy, A.; Lundberg, H.; Kärkäs, M. D. Organic Electrosynthesis: Applications in Complex Molecule Synthesis. *ChemElectroChem* **2019**, *6* (16), 4067–4092. https://doi.org/10.1002/celc.201900435.

(8) Moeller, K. D. Synthetic Applications of Anodic Electrochemistry. *Tetrahedron* **2000**, *56* (49), 9527–9554. https://doi.org/10.1016/S0040-4020(00)00840-1.

(9) Wu, T.; Moeller, K. D. Organic Electrochemistry: Expanding the Scope of Paired Reactions. *Angew. Chemie* **2021**, *133* (23), 12993–13000. https://doi.org/10.1002/ange.202100193.

(10) Kärkäs, M. D. Electrochemical Strategies for C-H Functionalization and C-N Bond Formation. *Chem. Soc. Rev.* **2018**, *47* (15), 5786–5865. https://doi.org/10.1039/c7cs00619e.

(11) Jiang, Y.; Xu, K.; Zeng, C. Use of Electrochemistry in the Synthesis of Heterocyclic Structures. *Chem. Rev.* **2018**, *118* (9), 4485–4540. https://doi.org/10.1021/acs.chemrev.7b00271.

(12) MacKay, A. S.; Payne, R. J.; Malins, L. R. Electrochemistry for the Chemoselective Modification of Peptides and Proteins. *J. Am. Chem. Soc.* **2022**, *144* (1), 23–41. https://doi.org/10.1021/jacs.1c11185.

(13) Rosen, B. R.; Werner, E. W.; Brien, A. G. O.; Baran, P. S. Total Synthesis of Dixiamycin B by Electrochemical Oxidation. *J. Am. Chem. Soc.* **2014**, *136* (15), 5571–5574. https://doi.org/10.1021/ja5013323.

(14) Horn, E. J.; Rosen, B. R.; Chen, Y.; Tang, J.; Chen, K.; Eastgate, M. D.; Baran, P. S. Scalable and Sustainable Electrochemical Allylic C-H Oxidation. *Nature* **2016**, *533* (7601), 77–81. https://doi.org/10.1038/nature17431.

(15) Kawamata, Y.; Yan, M.; Liu, Z.; Bao, D. H.; Chen, J.; Starr, J. T.; Baran, P. S. Scalable, Electrochemical Oxidation of Unactivated C-H Bonds. *J. Am. Chem. Soc.* **2017**, *139* (22), 7448–7451. https://doi.org/10.1021/jacs.7b03539.

(16) Li, X.; Bai, F.; Liu, C.; Ma, X.; Gu, C.; Dai, B. Selective Electrochemical Oxygenation of Alkylarenes to Carbonyls. *Org. Lett.* **2021**, *23* (19), 7445–7449.

https://doi.org/10.1021/acs.orglett.1c02651.

(17) Sun, Y.; Li, X.; Yang, M.; Xu, W.; Xie, J.; Ding, M. Highly Selective Electrocatalytic Oxidation of Benzyl C-H Using Water as Safe and Sustainable Oxygen Source. *Green Chem.* **2020**, *22* (21), 7543–7551. https://doi.org/10.1039/d0gc01871f.

(18) Marko, J. A.; Durgham, A.; Bretz, S. L.; Liu, W. Electrochemical Benzylic Oxidation of C-H Bonds. *Chem. Commun.* **2019**, *55* (7), 937–940. https://doi.org/10.1039/c8cc08768g.

(19) Zeng, C. C.; Zhang, N. T.; Lam, C. M.; Little, R. D. Novel Triarylimidazole Redox Catalysts: Synthesis, Electrochemical Properties, and Applicability to Electrooxidative C-H Activation. *Org. Lett.* **2012**, *14* (5), 1314–1317. https://doi.org/10.1021/ol300195c.

(20) Das, A.; Nutting, J. E.; Stahl, S. S. Electrochemical C-H Oxygenation and Alcohol Dehydrogenation Involving Fe-Oxo Species Using Water as the Oxygen Source. *Chem. Sci.* **2019**, *10* (32), 7542–7548. https://doi.org/10.1039/c9sc02609f.

(21) Han, X.; Wang, K.; Zhang, G.; Gao, W.; Chen, J. Application of the Electrochemical Oxygen Reduction Reaction (ORR) in Organic Synthesis. *Adv. Synth. Catal.* **2019**, *361* (12), 2804–2824. https://doi.org/10.1002/adsc.201900003.

(22) Jud, W.; Kappe, C. O.; Cantillo, D. One-pot Multistep Electrochemical Strategy for the Modular Synthesis of Epoxides, Glycols, and Aldehydes from Alkenes. *Electrochem. Sci. Adv.* **2021**, *1* (3). https://doi.org/10.1002/elsa.202100002.

(23) Balaganesh, M.; Lawrence, S.; Christopher, C.; John Bosco, A.; Kulangiappar, K.; Raj, K. J. S. Nitrate Mediated Oxidation of P-Xylene by Emulsion Electrolysis. *Electrochim. Acta* **2013**, *111*, 384–389. https://doi.org/10.1016/j.electacta.2013.08.020.

(24) Wang, F.; Rafiee, M.; Stahl, S. S. Electrochemical Functional-Group-Tolerant Shono-Type Oxidation of Cyclic Carbamates Enabled by Aminoxyl Mediators. *Angew. Chemie - Int. Ed.* **2018**, *57* (22), 6686–6690. https://doi.org/10.1002/anie.201803539.

(25) Maalouf, J. H.; Jin, K.; Yang, D.; Limaye, A. M.; Manthiram, K. Kinetic Analysis of Electrochemical Lactonization of Ketones Using Water as the Oxygen Atom Source. *ACS Catal.* **2020**, *10* (10), 5750–5756. https://doi.org/10.1021/acscatal.0c00931.

(26) Lum, Y.; Huang, J. E.; Wang, Z.; Luo, M.; Nam, D. H.; Leow, W. R.; Chen, B.; Wicks, J.; Li, Y. C.; Wang, Y.; Dinh, C. T.; Li, J.; Zhuang, T. T.; Li, F.; Sham, T. K.; Sinton, D.; Sargent, E. H. Tuning OH Binding Energy Enables Selective Electrochemical Oxidation of Ethylene to Ethylene Glycol. *Nat. Catal.* **2020**, *3* (1), 14–22. https://doi.org/10.1038/s41929-019-0386-4.

(27) Jin, K.; Maalouf, J. H.; Lazouski, N.; Corbin, N.; Yang, D.; Manthiram, K. Epoxidation of Cyclooctene Using Water as the Oxygen Atom Source at Manganese Oxide Electrocatalysts. *J. Am. Chem. Soc.* **2019**, *141* (15), 6413–6418. https://doi.org/10.1021/jacs.9b02345.

(28) Leow, W. R.; Lum, Y.; Ozden, A.; Wang, Y.; Nam, D. H.; Chen, B.; Wicks, J.; Zhuang, T. T.; Li, F.; Sinton, D.; Sargent, E. H. Chloride-Mediated Selective Electrosynthesis of Ethylene and Propylene Oxides at High Current Density. *Science (80-.).* **2020**, *368* (6496), 1228–1233. https://doi.org/10.1126/science.aaz8459.

(29) Lin, X.; Zhou, Z.; Li, Q.; Xu, D.; Xia, S.-Y.; Leng, B.-L.; Zhai, G.-Y.; Zhang, S.-N.; Sun, L.-H.; Zhao, G.; Chen, J.-S.; Li, X.-H. Direct Oxygen Transfer from H2O to Cyclooctene over Electron-Rich RuO2 Nanocrystals for Epoxidation and Hydrogen Evolution. *Angew. Chemie Int. Ed.* **2022**, *61* (35). https://doi.org/10.1002/anie.202207108.

(30) Chung, M.; Jin, K.; Zeng, J. S.; Ton, T. N.; Manthiram, K. Tuning Single-Atom Dopants on Manganese Oxide for Selective Electrocatalytic Cyclooctene Epoxidation. *J. Am. Chem. Soc.* **2022**, *144* (38), 17416–17422. https://doi.org/10.1021/jacs.2c04711.

(31) Leduc, J. A. M. Electrochemical Process for the Production of Organic Oxides. U.S. Patent no. 3,288,692, 1966.

(32) Torii, S.; Uneyama, K.; Tanaka, H.; Yamanaka, T.; Yasuda, T.; Ono, M.; Kohmoto, Y. Efficient Conversion of Olefins into Epoxides, Bromohydrins, and Dibromides with Sodium Bromide in Water-Organic Solvent Electrolysis Systems. *J. Org. Chem.* **1981**, *46* (16), 3312–3315. https://doi.org/10.1021/jo00329a032.

(33) Van der Eijk, J. M.; Peters, T. J.; de Wit, N.; Colijn, H. A. Electrochemical Epoxidation of Olefins. *Catal. Today* **1988**, *3* (2–3), 259–266. https://doi.org/10.1016/0920-

5861(88)87014-7.

(34) Rossen, K.; Volante, R. P.; Reider, P. J. A Highly Diastereoselective Electrochemical Epoxidation. *Tetrahedron Lett.* **1997**, *38* (5), 777–778. https://doi.org/10.1016/S0040-4039(96)02445-8.

(35) Tanaka, H.; Kuroboshi, M.; Takeda, H.; Kanda, H.; Torii, S. Electrochemical Asymmetric Epoxidation of Olefins by Using an Optically Active Mn-Salen Complex. *J. Electroanal. Chem.* **2001**, *507* (1–2), 75–81. https://doi.org/10.1016/S0022-0728(01)00387-4.

(36) Zimmer, A.; Mönter, D.; Reschetilowski, W. Catalytic Epoxidation with Electrochemically in Situ Generated Hydrogen Peroxide. *J. Appl. Electrochem.* **2003**, *33* (10), 933–937. https://doi.org/10.1023/A:1025881213041.

(37) Espinal, L.; Suib, S. L.; Rusling, J. F. Electrochemical Catalysis of Styrene Epoxidation with Films of MnO 2 Nanoparticles and H2O2. *J. Am. Chem. Soc.* **2004**, *126* (24), 7676–7682. https://doi.org/10.1021/ja048940x.

(38) Tang, M. C. Y.; Wong, K. Y.; Chan, T. H. Electrosynthesis of Hydrogen Peroxide in Room Temperature Ionic Liquids and in Situ Epoxidation of Alkenes. *Chem. Commun.* **2005**, No. 10, 1345–1347. https://doi.org/10.1039/b416837b.

(39) Marco-Contelles, J.; Molina, M. T.; Anjum, S. Naturally Occurring Cyclohexane Epoxides: Sources, Biological Activities and Synthesis. *Chem. Rev.* **2004**, *104* (6), 2857–2899. https://doi.org/10.1021/cr980013j.

(40) Gomes, A. R.; Varela, C. L.; Tavares-da-Silva, E. J.; Roleira, F. M. F. Epoxide Containing Molecules: A Good or a Bad Drug Design Approach. *Eur. J. Med. Chem.* **2020**, *201*. https://doi.org/10.1016/j.ejmech.2020.112327.

(41) Davis, R. L.; Stiller, J.; Naicker, T.; Jiang, H.; Jørgensen, K. A. Asymmetric Organocatalytic Epoxidations: Reactions, Scope, Mechanisms, and Applications. *Angew. Chemie - Int. Ed.* **2014**, *53* (29), 7406–7426. https://doi.org/10.1002/anie.201400241.

(42) Moschona, F.; Savvopoulou, I.; Tsitopoulou, M.; Tataraki, D.; Rassias, G. Epoxide Syntheses and Ring-Opening Reactions in Drug Development. *Catalysts* **2020**, *10* (10), 1117. https://doi.org/10.3390/catal10101117.

(43) Nijhuis, T. A.; Makkee, M.; Moulijn, J. A.; Weckhuysen, B. M. The Production of Propene Oxide: Catalytic Processes and Recent Developments. *Ind. Eng. Chem. Res.* **2006**, *45* (10), 3447–3459. https://doi.org/10.1021/ie0513090.

(44) Kostopoulos, N.; Banse, F.; Fave, C.; Anxolabéhère-Mallart, E. Modulating Alkene Reactivity from Oxygenation to Halogenation via Electrochemical O2 Activation by Mn Porphyrin. *Chem. Commun.* **2021**, *57* (10), 1198–1201. https://doi.org/10.1039/d0cc07531k.

(45) Jirkovský, J. S.; Busch, M.; Ahlberg, E.; Panas, I.; Krtil, P. Switching on the Electrocatalytic Ethene Epoxidation on Nanocrystalline RuO2. *J. Am. Chem. Soc.* **2011**, *133* (15), 5882–5892. https://doi.org/10.1021/ja109955w.

(46) Grimaud, A.; Diaz-Morales, O.; Han, B.; Hong, W. T.; Lee, Y. L.; Giordano, L.; Stoerzinger, K. A.; Koper, M. T. M.; Shao-Horn, Y. Activating Lattice Oxygen Redox Reactions in Metal Oxides to Catalyse Oxygen Evolution. *Nat. Chem.* **2017**, *9* (5), 457–465. https://doi.org/10.1038/nchem.2695.

(47) Grimaud, A.; Hong, W. T.; Shao-Horn, Y.; Tarascon, J. M. Anionic Redox Processes for Electrochemical Devices. *Nat. Mater.* **2016**, *15* (2), 121–126. https://doi.org/10.1038/nmat4551.

(48) Grimaud, A.; May, K. J.; Carlton, C. E.; Lee, Y. L.; Risch, M.; Hong, W. T.; Zhou, J.; Shao-Horn, Y. Double Perovskites as a Family of Highly Active Catalysts for Oxygen Evolution in Alkaline Solution. *Nat. Commun.* **2013**, *4* (May), 1–7. https://doi.org/10.1038/ncomms3439.

(49) Zhao, Y.; Deng, C.; Tang, D.; Ding, L.; Zhang, Y.; Sheng, H.; Ji, H.; Song, W.; Ma, W.; Chen, C.; Zhao, J. α-Fe2O3 as a Versatile and Efficient Oxygen Atom Transfer Catalyst in Combination with H2O as the Oxygen Source. *Nat. Catal.* **2021**, *4*, 684–691. https://doi.org/10.1038/s41929-021-00659-1.

(50) Dubouis, N.; Serva, A.; Berthin, R.; Jeanmairet, G.; Porcheron, B.; Salager, E.; Salanne, M.; Grimaud, A. Tuning Water Reduction through Controlled Nanoconfinement within an Organic Liquid Matrix. *Nat. Catal.* **2020**, *3* (8), 656–663. https://doi.org/10.1038/s41929-

020-0482-5.

(51) Hollóczki, O.; Macchieraldo, R.; Gleede, B.; Waldvogel, S. R.; Kirchner, B. Interfacial Domain Formation Enhances Electrochemical Synthesis. *J. Phys. Chem. Lett.* **2019**, *10* (6), 1192–1197. https://doi.org/10.1021/acs.jpclett.9b00112.

(52) Blanco, D. E.; Atwi, R.; Sethuraman, S.; Lasri, A.; Morales, J.; Rajput, N. N.; Modestino, M. A. Effect of Electrolyte Cations on Organic Electrosynthesis: The Case of Adiponitrile Electrochemical Production. *J. Electrochem. Soc.* **2020**, *167* (15), 155526. https://doi.org/10.1149/1945-7111/abc766.

(53) Yang, C.; Fontaine, O.; Tarascon, J. M.; Grimaud, A. Chemical Recognition of Active Oxygen Species on the Surface of Oxygen Evolution Reaction Electrocatalysts. *Angew. Chemie - Int. Ed.* **2017**, *56* (30), 8652–8656. https://doi.org/10.1002/anie.201701984.

(54) Görlin, M.; Halldin Stenlid, J.; Koroidov, S.; Wang, H. Y.; Börner, M.; Shipilin, M.; Kalinko, A.; Murzin, V.; Safonova, O. V.; Nachtegaal, M.; Uheida, A.; Dutta, J.; Bauer, M.; Nilsson, A.; Diaz-Morales, O. Key Activity Descriptors of Nickel-Iron Oxygen Evolution Electrocatalysts in the Presence of Alkali Metal Cations. *Nat. Commun.* **2020**, *11* (1), 1–11. https://doi.org/10.1038/s41467-020-19729-2.

(55) Wagner, D.; Gerischer, H. The Influence of the Water Activity in Acetonitrile on the Formation and Reduction of an Oxide Layer on Gold. *J. Electroanal. Chem.* **1989**, *258* (1), 127–137. https://doi.org/10.1016/0022-0728(89)85167-8.

(56) Ledezma-Yanez, I.; Koper, M. T. M. Influence of Water on the Hydrogen Evolution Reaction on a Gold Electrode in Acetonitrile Solution. *J. Electroanal. Chem.* **2017**, *793*, 18–24. https://doi.org/10.1016/j.jelechem.2016.08.018.

(57) Dubouis, N.; Serva, A.; Salager, E.; Deschamps, M.; Salanne, M.; Grimaud, A. The Fate of Water at the Electrochemical Interfaces: Electrochemical Behavior of Free Water Versus Coordinating Water. *J. Phys. Chem. Lett.* **2018**, *9* (23), 6683–6688. https://doi.org/10.1021/acs.jpclett.8b03066.

(58) Serva, A.; Dubouis, N.; Grimaud, A.; Salanne, M. Confining Water in Ionic and Organic Solvents to Tune Its Adsorption and Reactivity at Electrified Interfaces. *Acc. Chem. Res.*

2021, *54* (4), 1034–1042. https://doi.org/10.1021/acs.accounts.0c00795.

(59) Xu, X.; Makaraviciute, A.; Pettersson, J.; Zhang, S. L.; Nyholm, L.; Zhang, Z. Revisiting the Factors Influencing Gold Electrodes Prepared Using Cyclic Voltammetry. *Sensors Actuators, B Chem.* **2019**, *283* (August 2018), 146–153. https://doi.org/10.1016/j.snb.2018.12.008.

(60) Kasian, O.; Kulyk, N.; Mingers, A.; Zeradjanin, A. R.; Mayrhofer, K. J. J.; Cherevko, S. Electrochemical Dissolution of Gold in Presence of Chloride and Bromide Traces Studied by On-Line Electrochemical Inductively Coupled Plasma Mass Spectrometry. *Electrochim. Acta* **2016**, *222*, 1056–1063. https://doi.org/10.1016/j.electacta.2016.11.074.

(61) Sauerbrey, G. Verwendung von Schwingquarzen Zur Wägung Dünner Schichten Und Zur Mikrowägung. *Zeitschrift für Phys.* **1959**, *155* (2), 206–222. https://doi.org/10.1007/BF01337937.

(62) Hillman, A. R. The EQCM: Electrogravimetry with a Light Touch. *J. Solid State Electrochem.* **2011**, *15* (7–8), 1647–1660. https://doi.org/10.1007/s10008-011-1371-2.

(63) Shpigel, N.; Levi, M. D.; Aurbach, D. EQCM-D Technique for Complex Mechanical Characterization of Energy Storage Electrodes: Background and Practical Guide. *Energy Storage Mater.* **2019**, *21* (January), 399–413. https://doi.org/10.1016/j.ensm.2019.05.026.

(64) Jašíková, L.; Roithová, J. Interaction of the Gold(I) Cation Au(PMe 3) + with Unsaturated Hydrocarbons. *Organometallics* **2012**, *31* (5), 1935–1942. https://doi.org/10.1021/om2012387.

(65) Chambrier, I.; Rocchigiani, L.; Hughes, D. L.; Budzelaar, P. M. H.; Bochmann, M. Thermally Stable Gold(III) Alkene and Alkyne Complexes: Synthesis, Structures, and Assessment of the Trans-Influence on Gold–Ligand Bond Enthalpies. *Chem. - A Eur. J.* **2018**, *24* (44), 11467–11474. https://doi.org/10.1002/chem.201802160.

(66) Haiss, W.; Thanh, N. T. K.; Aveyard, J.; Fernig, D. G. Determination of Size and Concentration of Gold Nanoparticles from UV−Vis Spectra. *Anal. Chem.* **2007**, *79* (11), 4215–4221. https://doi.org/10.1021/ac0702084.

(67) Hendel, T.; Wuithschick, M.; Kettemann, F.; Birnbaum, A.; Rademann, K.; Polte, J. In

Situ Determination of Colloidal Gold Concentrations with UV–Vis Spectroscopy: Limitations and Perspectives. *Anal. Chem.* **2014**, *86* (22), 11115–11124. https://doi.org/10.1021/ac502053s.

(68) Chiarucci, M.; Bandini, M. New Developments in Gold-Catalyzed Manipulation of Inactivated Alkenes. *Beilstein J. Org. Chem.* **2013**, *9* (Figure 1), 2586–2614. https://doi.org/10.3762/bjoc.9.294.

(69) Zhang, R.; Pearce, P. E.; Duan, Y.; Dubouis, N.; Marchandier, T.; Grimaud, A. Importance of Water Structure and Catalyst-Electrolyte Interface on the Design of Water Splitting Catalysts. *Chem. Mater.* **2019**, *31* (20), 8248–8259. https://doi.org/10.1021/acs.chemmater.9b02318.

(70) Duan, Y.; Dubouis, N.; Huang, J.; Dalla Corte, D. A.; Pimenta, V.; Xu, Z. J.; Grimaud, A. Revealing the Impact of Electrolyte Composition for Co-Based Water Oxidation Catalysts by the Study of Reaction Kinetics Parameters. *ACS Catal.* **2020**, *10* (7), 4160–4170. https://doi.org/10.1021/acscatal.0c00490.

(71) Ranninger, J.; Mayrhofer, K. J. J.; Berkes, B. B. The Crucial Role of Water in the Stability and Electrocatalytic Activity of Pt Electrodes. *J. Phys. Chem. C* **2021**, *125* (24), 13254–13263. https://doi.org/10.1021/acs.jpcc.1c02124.

(72) Valleau, J. P.; J.M., T. Nonphysical Sampling Distributions in Monte Carlo Free-Energy Estimation: Umbrella Sampling. *J. Comput. Phys.* **1977**, *23* (2), 187–199.

(73) Kawamata, Y.; Baran, P. S. Electrosynthesis : Sustainability Is Not Enough. *Joule* **2020**, *4* (4), 701–704. https://doi.org/10.1016/j.joule.2020.02.002.

(74) Marin-Laflèche, A.; Haefele, M.; Scalfi, L.; Coretti, A.; Dufils, T.; Jeanmairet, G.; Reed, S.; Serva, A.; Berthin, R.; Bacon, C.; Bonella, S.; Rotenberg, B.; Madden, P.; Salanne, M. MetalWalls: A Classical Molecular Dynamics Software Dedicated to the Simulation of Electrochemical Systems. *J. Open Source Softw.* **2020**, *5* (53), 2373. https://doi.org/10.21105/joss.02373.

(75) Grabuleda, X.; Jaime, C.; Kollmans, P. A. Molecular Dynamics Simulation Studies of Liquid Acetonitrile: New Six-site Model. *J. Comput. Chem.* **2000**, *21*, 901–908.

(76) Berendsen, H. J. C.; Grigera, J. R.; Straatsma, T. P. The Missing Term in Effective Pair Potentials. *J. Phys. Chem.* **1987**, *91* (24), 6269–6271. https://doi.org/10.1021/j100308a038.

(77) Liu, X.; Zhang, S.; Zhou, G.; Wu, G.; Yuan, X.; Yao, X. New Force Field for Molecular Simulation of Guanidinium-Based Ionic Liquids. *J. Phys. Chem. B* **2006**, *110* (24), 12062–12071. https://doi.org/10.1021/jp060834p.

(78) Bhowmik, D.; Malikova, N.; Mériguet, G.; Bernard, O.; Teixeira, J.; Turq, P. Aqueous Solutions of Tetraalkylammonium Halides: Ion Hydration, Dynamics and Ion-Ion Interactions in Light of Steric Effects. *Phys. Chem. Chem. Phys.* **2014**, *16* (26), 13447–13457. https://doi.org/10.1039/c4cp01164c.

(79) Åqvist, J. Ion-Water Interaction Potentials Derived from Free Energy Perturbation Simulations. *J. Phys. Chem.* **1990**, *94* (21), 8021–8024. https://doi.org/10.1021/j100384a009.

(80) Nosé, S. A Unified Formulation of the Constant Temperature Molecular Dynamics Methods. *J. Chem. Phys.* **1984**, *81* (1), 511–519. https://doi.org/10.1063/1.447334.

(81) Evans, D. J.; Holian, B. L. The Nose-Hoover Thermostat. *J. Chem. Phys.* **1985**, *83* (8), 4069–4074. https://doi.org/10.1063/1.449071.

(82) Martínez, L.; Andrade, R.; Birgin, E. G.; Martínez, J. M. PACKMOL: A Package for Building Initial Configurations for Molecular Dynamics Simulations. *J. Comput. Chem.* **2009**, *30* (13), 2157–2164. https://doi.org/10.1002/jcc.21224.

(83) Ryckaert, J. P.; Ciccotti, G.; Berendsen, H. J. C. Numerical Integration of the Cartesian Equations of Motion of a System with Constraints: Molecular Dynamics of n-Alkanes. *J. Comput. Phys.* **1977**, *23* (3), 327–341. https://doi.org/10.1016/0021-9991(77)90098-5.

(84) Ciccotti, G.; Ferrario, M.; Ryckaert, J.-P. Molecular Dynamics of Rigid Systems in Cartesian Coordinates A General Formulation. *Mol. Phys.* **1982**, *47* (6), 1253–1264. https://doi.org/10.1080/00268978200100942.

(85) Brehm, M.; Kirchner, B. TRAVIS - A Free Analyzer and Visualizer for Monte Carlo and Molecular Dynamics Trajectories. *J. Chem. Inf. Model.* **2011**, *51* (8), 2007–2023.

https://doi.org/10.1021/ci200217w.

(86) Brehm, M.; Weber, H.; Thomas, M.; Hollóczki, O.; Kirchner, B. Domain Analysis in Nanostructured Liquids: A Post-Molecular Dynamics Study at the Example of Ionic Liquids. *ChemPhysChem* **2015**, *16* (15), 3271–3277. https://doi.org/10.1002/cphc.201500471.

(87) Humphrey, W.; Dalke, A.; Schulten, K. VMD: Visual Molecular Dynamics. *J. Mol. Graph.* **1996**, *14* (1), 33–38. https://doi.org/10.1016/0263-7855(96)00018-5.

(88) Reed, S. K.; Lanning, O. J.; Madden, P. A. Electrochemical Interface between an Ionic Liquid and a Model Metallic Electrode. *J. Chem. Phys.* **2007**, *126* (8). https://doi.org/10.1063/1.2464084.

(89) Siepmann, J. I.; Sprik, M. Influence of Surface Topology and Electrostatic Potential on Water/Electrode Systems. *J. Chem. Phys.* **1995**, *102* (1), 511–524. https://doi.org/10.1063/1.469429.

(90) Berg, A.; Peter, C.; Johnston, K. Evaluation and Optimization of Interface Force Fields for Water on Gold Surfaces. *J. Chem. Theory Comput.* **2017**, *13* (11), 5610–5623. https://doi.org/10.1021/acs.jctc.7b00612.

(91) Gingrich, T. R.; Wilson, M. On the Ewald Summation of Gaussian Charges for the Simulation of Metallic Surfaces. *Chem. Phys. Lett.* **2010**, *500* (1–3), 178–183. https://doi.org/10.1016/j.cplett.2010.10.010.

(92) Serva, A.; Scalfi, L.; Rotenberg, B.; Salanne, M. Effect of the Metallicity on the Capacitance of Gold-Aqueous Sodium Chloride Interfaces. *J. Chem. Phys.* **2021**, *155* (4), 1–8. https://doi.org/10.1063/5.0060316.

(93) Tribello, G. A.; Bonomi, M.; Branduardi, D.; Camilloni, C.; Bussi, G. PLUMED 2: New Feathers for an Old Bird. *Comput. Phys. Commun.* **2014**, *185* (2), 604–613. https://doi.org/10.1016/j.cpc.2013.09.018.

TABLE OF CONTENTS GRAPHIC